Dynamic Coordinated Control During Mode Transition Process for a Plug-In Hybrid Electric Vehicle

YANZHAO SU[1], MINGHUI HU[1], (Member, IEEE), LING SU[2],
DATONG QIN[1], (Member, IEEE), AND YI ZHANG[3]

[1]State Key Laboratory of Mechanical Transmissions, Chongqing University, Chongqing 400044, China
[2]Chongqing Changan Automobile Co., Ltd., Chongqing 401120, China
[3]Department of Mechanical Engineering, University of Michigan–Dearborn, Dearborn, MI 48128, USA

Corresponding author: Minghui Hu (minghui_h@163.com)

ABSTRACT The fuel-saving advantages of plug-in hybrid electric vehicles can be improved using optimized configurations and appropriate energy management strategies. However, the noticeable jerks and vibrations of the powertrain can be generated by torque fluctuations in the mode transition (MT), especially, the transition from electric mode to hybrid driving mode that involves engine starting. To address this problem, this paper proposes a dynamic coordinated control strategy that synergizes real-time discrete motor torque change rate limitation (TCRL) and active damping feedback compensation (ADFC) control. First, a detailed vehicle powertrain simulation model is established and validated. The relevant problems in the MT are analyzed by the experimental data. Second, the algorithms relevant to the torque distribution of the power source and the real-time discrete motor TCRL are designed from the kinematic and dynamic relationships of the powertrain at each stage. Considering model inaccuracies, system parameter uncertainties, and load changes, an ADFC is designed based on real-time robust drive shaft torque observer. Moreover, the optimal observer gain is obtained by genetic algorithm under the linear matrix inequalities (LMIs) restriction to improve the robustness of the observer. Finally, the simulation and experimental results indicate that the proposed TCRL–ADFC method can effectively reduce the powertrain shocks and improve the ride comfort.

INDEX TERMS Active damping feedback compensation, coordinated control, genetic algorithm, mode transition, torque change rate limitation.

I. INTRODUCTION

With the energy crisis and environmental pollution becoming important, new energy vehicles have played an important role in the development of the car industry [1]. Engine and wheel speeds can be decoupled by using motors' speed regulation function, which ensures that the engine operates within a high-efficiency region in a power-split plug-in hybrid electric vehicle (PS-PHEV). Note that all abbreviations and their explanations in this paper are listed in Table 7 of Appendix B. As a result, this technology has received broad attention and interest from major car manufacturers [2].

The associate editor coordinating the review of this manuscript and approving it for publication was Danping He.

The fuel consumption of hybrid electric vehicle can be effectively reduced by using its configuration design [3] and an appropriate energy management strategy [4]. However, since a compound power-split mechanism is directly connected to the engine, noticeable jerks and vibrations of the powertrain can be generated by engine ripple torque (ERT) during the mode transition (MT) process, especially during the transition from electric vehicle (EV) mode to electric continuous variable transmission (ECVT) mode [5]–[12], which involves engine starting. When the motors starts the engine, since the initial intake manifold pressure is close to atmospheric pressure, the ERT, especially the item of the cylinder pressure ripple torque, is high, which is directly transmitted to the wheels through the transmission chain, reducing

driving comfort. Besides, since the data map in the model is mostly obtained by a series of static experiments and the estimation models are mostly based on simplified theoretical formulas, these data maps and estimation models can lead to model errors, which are defined as model inaccuracies (MI). In addition, vehicle mass, road slope, system elastic damping, etc. are mostly set as constant values in the control model, but in fact, they are some varying parameters within a certain range, which are defined as the system parameter uncertainties (SPU). However, the MI and SPU will affect the control accuracy and reduce driving comfort to some extent.

To address the issue of MT, some methods have been enforced to reduce the shocks and vibrations during MT process. These methods include constructing an engine transient torque interpolation table [6]–[8], setting up a reduced-order engine thermodynamic model [9], [10], creating an engine torque ripple approximation function [11], and establishing an engine torque estimation model from kinematic and kinetic relationships of the planetary gears [12]. Then compensation torques of motors are used to reduce the system shocks following the above methods. However, in the implementation of such schemes, the influences of MI and SPU have been neglected. Zeng restricted the torques' change of the power source based on model prediction theory to reduce vehicle jerk [13] and proposed a strategy in which the first motor adopted feedforward and feedback method and the second motor adopted torque compensation control by means of the engine torque estimation [14]. However, the dynamic simulation model (also known as plant model) ignored the ERT, MI, and SPU. Dynamic programming algorithm [15], [16] was used to obtain the optimal motor torques, brake pressure and engine start-up speed trajectory. However, this method uses known data to solve the optimal value problem, which is difficult to be directly used in practical applications.

In addition, an active damping based on weighted feedback control method [17], and an active damping proportion and differentiation (PD) control method [12] have been proposed to reduce the torque fluctuations at the wheels. However, the MI and SPU of the vehicle powertrain were not taken into consideration by these methods, which may affect the robustness for practical applications. Several coordinated control strategies have been proposed to solve the system shock problem caused by the system disturbances such as clutch friction torques and engine fluctuation torque errors. These methods include the online parameter identification using disturbance observers [18], fuzzy adaptive control using sliding variable structure [19], motor speed tracking control based on H_∞ robust control theory [20], and robust controllers designed by using the $m\mu$ synthesis method [21], [22]. However, they neglected the ERTs and mainly solved the coordination control problems in the clutch operating process for a parallel hybrid electric vehicle. Zhou *et al.* [23] estimated the brake pressure and drive shaft torque by using robust observer for process of starting engine assisted by a brake. However, the real-time estimation algorithm for wheel speed is not

designed and the dynamic coordinated control in the MT is not involved. Besides, references [8], [12] and [24] are all related to the study of MT process for the same vehicle powertrain structure as in this article. However, the control method in this paper is significantly different from the previous researches.

Since the relationship between vehicular jerk and the torque change rate of a power source can be obtained by the powertrain dynamic model, it is possible to limit the motor torque change rate at different stages during the MT process by the preset jerk to realize torque coordination control. However, factors such as MI in engine model estimation and SPU in system damping and inertia make it more difficult to reduce the system torque fluctuations when motor torque change rate limitation (TCRL) is used only. As a result, these fluctuating torques will be transferred to the wheels through the transmission shaft, which will affect driving comfort. To address these problems, considering MI and SPU, a drive shaft torque estimation (DSTE) observer will be designed, and two motors will be employed to carry out torque compensation control to reduce jerk and vibration transmitted to the wheels. We will call this control as an active damping feedback compensation (ADFC) control.

In the authors' previous research [25], we proposed a coordinated control strategy that includes a staged engine torque feedforward and feedback estimation and an active damping feedback compensation. However, this method does not involve the influence of the motor torque change rate and error properties of active damping observer do not be analyzed. The gain of DSTE observer is not optimized either. Moreover, the proposed control method has not been verified by experiments. Therefore, based on these factors, in this paper we develop a dynamic coordinated control strategy (DCCS) that synergizes real-time discrete motor TCRL and ADFC based on optimized DSTE during the MT to reduce the shocks and vibrations of the vehicle transmission system. There are three main contributions in this paper: *1)* Algorithms of the power source torque distribution and real-time discrete motor TCRL are designed from the kinematic and dynamic relationships obtained by lever diagrams constructed at each stage during MT. *2)* Considering MI, SPU, and load changes, an ADFC is developed for all working stages. Error properties of active damping observer are analyzed and the optimal observer gain is obtained by genetic algorithm under the LMIs restriction to improve the robustness of the observer. *3)* A detailed vehicle powertrain plant model is established and validated. Moreover, the relevant experimental verification of DCCS is completed. Using the above-mentioned method, the proposed DCCS is suitable for all working stages, and can possess good real-time and robustness.

The remaining sections of this study are organized as follows: The vehicle powertrain simulation model is firstly established in Section II. In Section III, the MT is analyzed and relevant problems are described by experiment data. Then, the DCCS is designed in Section IV and DCCS is
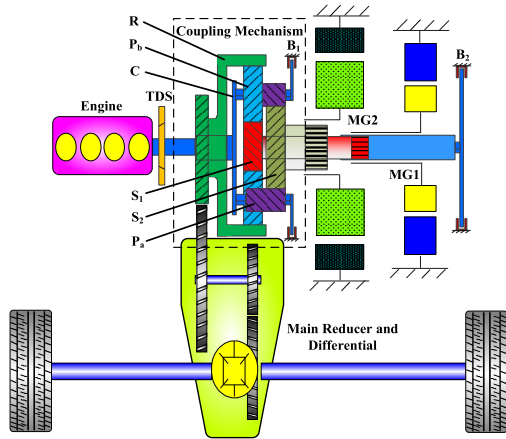
FIGURE 1. Schematic of a compound power-split powertrain.

simulated in Section V. In Section VI, experiments are performed by using a PS-PHEV. Finally, concluding remarks are outlined in Section VII.

II. POWERTRAIN DYNAMIC MODELING

A compound power-split powertrain with a Ravigneaux planetary gear train (seen in Fig.1) is studied in this paper. The small sun S_1 connects with the small motor 1 (MG1), which can be locked by the brake B_2. The big sun S_2 connects with the big motor 2 (MG2). P_a and P_b are the rear and front planetary gears, respectively. C is the sharing carrier that is connected to the engine by the torsional damper spring (TDS), which can be locked by the brake B_1. R is the ring that is connected to main reducer. A plant model is established by using the *MATLAB/Simulink* environment as described next.

A. ENGINE RIPPLE TORQUE MODELING

The output torque T_{ERT} of the four-cylinder engine before engine flywheel is equal to the sum of four cylinders' torques with 180 degrees difference. The detailed equations can be referred in [9], [25].

$$T_{ERT} = \sum_i T_{cyl,i} = \sum_i \left(T_{P_i} + T_{I_i} + T_{F_i} \right) \qquad (1)$$

where $T_{cyl,i}$ is the corresponding ERT of the *i*-th cylinder ($i = 1, 2, 3, 4$), T_{P_i} is the cylinder pressure ripple torque, T_{I_i} is the inertia torque of the piston and connecting rod, and T_{F_i} is the piston and air valve friction torque.

In this paper, gas pressures at different throttle positions and some model parameters were obtained from an engine dynamic bench test in Fig. 2.

We will take the typical throttle position before and after ignition as examples to analyze ERTs. As illustrated in Fig. 3, the ERT of the motoring stage before engine ignition is plotted at different engine speeds when a throttle position is 6%. We can find that ERT before ignition fluctuates once every 180 degrees periodically in a 720-degree cycle. The positive peak torques at 200 rpm, 400 rpm and 600 rpm are greater than that at 800 rpm, and their negative peak torque is similar.
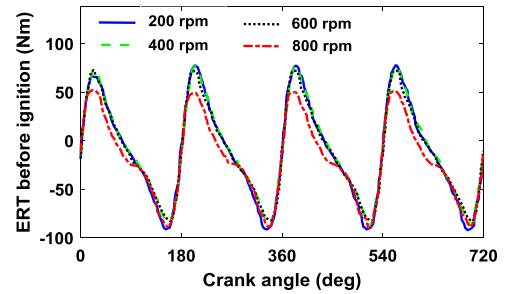

FIGURE 2. Engine experimental bench.

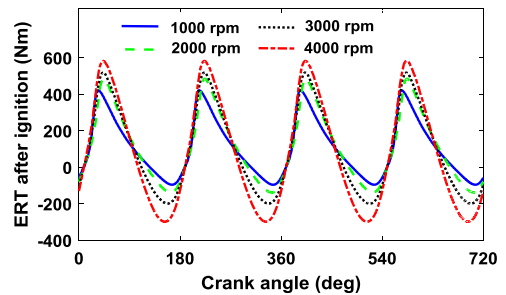**FIGURE 3.** ERT before engine ignition.

FIGURE 4. ERT after engine ignition.

Correspondingly, Fig. 4 depicts ERT of the firing stage after engine ignition at different speeds when a throttle position is 24%. We can also see that ERT of the firing stage has similar periodic fluctuations. The ERT peak torque increases with the increase of engine speed.

It is clear from these two figures that the ERT curves present significant periodic fluctuations. This means that the engine characteristics from the engine steady-state map cannot completely reflect the actual engine dynamic characteristics.

B. BATTERY-MOTOR MODELING AND VALIDATION

The battery-motor model includes the basic modules such as *battery*, simscape power system (*SPS*) *drives, converter,* and *permanent magnet (PM) synchronous motor drive* in the *Simscape toolbox* [25], [26]. Electromagnetic torque is calculated as follows:

$$T_{MG} = 1.5 p_s [\lambda_a i_q + (L_d - L_q) i_d i_q] \qquad (2)$$
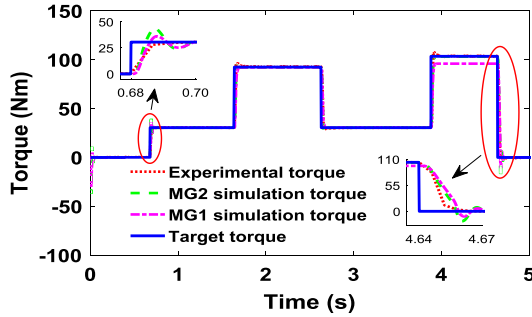
FIGURE 5. Motor dynamic test bench.

FIGURE 6. Motor torque following characteristics.

where p_s is the pole pair number, λ_a is the flux amplitude, L_q and L_d are inductances at the q-axis and d-axis, respectively, and i_q, i_d are currents at the q-axis and d-axis, respectively.

A PM synchronous motor test bench was built to verify the dynamic characteristics of the battery–motor model, as shown in Fig. 5. At room temperature of $25°$, the dynamometer's speed was stable at 2000rpm. The motor torque was sent step-by-step command as shown in Fig. 6. The two motors' models were simulated under the same conditions. We can see that both motors can well follow the target torques. Note that the MG1 torque does not reach 100Nm between 3.83s and 4.64s because the maximum torque limitation of MG1. In addition, the torque response time of the two motor models is basically consistent with the experimental results in Fig. 6. From these results, we can see that the simulation results are in good agreement with the experimental data, which verifies the effectiveness of the battery-motor model.

C. PLANETARY DYNAMIC MODEL AND VALIDATION

A pure torsional planetary dynamic model was built by using the lumped-parameter method [25], [27] to ensure that the dynamic characteristics of the compound power-split mechanism are close to those in actual environments, as shown in Fig. 7. Three coordinate systems in this model are set. *OXY* is the stationary coordinate system. *oxy* is the kinetic coordinate system, and $o_n\xi_n\eta_n$ is the moving coordinate system. θ, k, c, e, and h are the angular displacement, time-varying meshing stiffness, meshing damping, meshing error, and gear backlash, respectively. a and b are the planetary gears of rear row and front row, respectively.
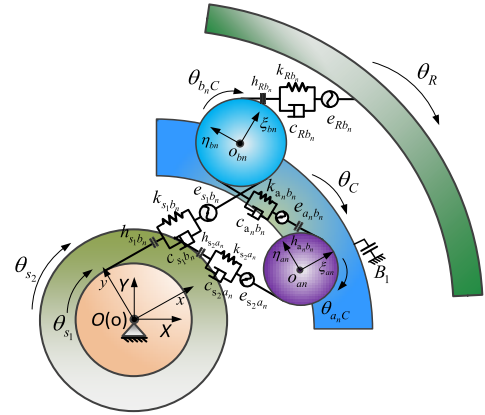

FIGURE 7. Pure torsional planetary dynamic model.

The motion formulas are given as follows:

$$I_{s_1}\ddot{\theta}_{s_1} = T_{s_1} + \sum_{n=1}^{N} F_{ys_1b_n} \cdot r_{s_1} \tag{3}$$

$$I_{s_2}\ddot{\theta}_{s_2} = T_{s_2} + \sum_{n=1}^{N} F_{ys_2a_n} \cdot r_{s_2} \tag{4}$$

$$I_{ce}\ddot{\theta}_C = T_C + \sum_{n=1}^{N} F_{ys_2a_n} \cdot \cos\alpha_{s_2} \cdot r_C$$
$$+ \sum_{n=1}^{N} F_{ys_1b_n} \cdot \cos\alpha_{s_1} \cdot r_C - \sum_{n=1}^{N} F_{yRb_n} \cdot \cos\alpha_r \cdot r_C \tag{5}$$

$$I_R\ddot{\theta}_R = \sum_{n=1}^{N} F_{yRb_n} \cdot r_R - T_L \tag{6}$$

$$I_a\ddot{\theta}_{a_nc} = F_{ya_nb_n} \cdot r_a - F_{ys_2a_n} \cdot r_a \tag{7}$$

$$I_b\ddot{\theta}_{b_nc} = F_{ya_nb_n} \cdot r_b - F_{yRb_n} \cdot r_b - F_{ys_1b_n} \cdot r_b \tag{8}$$

where I_{s_1}, I_{s_2}, I_R, I_a, I_b and I_C are inertias of S_1, S_2, ring, rear planet, front planet and carrier, respectively. $\ddot{\theta}_{s_1}$, $\ddot{\theta}_{s_2}$, $\ddot{\theta}_C$, $\ddot{\theta}_R$, $\ddot{\theta}_{a_nc}$ and $\ddot{\theta}_{b_nc}$ are the angular accelerations of S_1, S_2, carrier, ring, rear planet and front planet, respectively. T_{s_1}, T_{s_2}, T_C and T_L are torques of S_1, S_2, carrier and load at ring axle, respectively. $F_{ys_1b_n}$ and α_{s_1} are dynamic meshing force and meshing angle between S_1 and front planet, $F_{ys_2a_n}$ and α_{s_2} are dynamic meshing force and meshing angle between S_2 and rear planet, F_{yRb_n} and α_r are dynamic meshing force and meshing angle between ring and front planet, and $F_{ya_nb_n}$ is dynamic meshing force between rear planet and front planet. The dynamic meshing forces are given by [27]. r_{s_1}, r_{s_2}, r_C, r_R, r_a and r_b are base circle radiuses of S_1, S_2, carrier, ring, rear planet and front planet, respectively. $N(n)$ is planet number and $I_{ce} = I_C + NI_a + NI_b$.

In this model, we set the gear backlash to 100μm and the maximum error to 2μm. As shown in Fig. 8, ring torques of the plant model and simple model without dynamic meshing force [24] are in good agreement. Moreover, the plant model
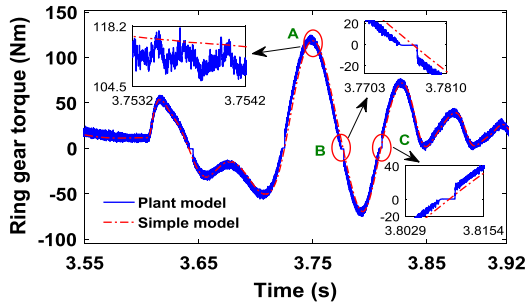
FIGURE 8. Pure torsional dynamic model validation.

can effectively reflect the dynamic torque characteristics of ring gear caused by meshing errors (shown in area A), time-varying meshing stiffness (shown in area A), and backlash (shown in areas B and C). These results verify the effectiveness of the pure torsional dynamic model.

D. BRAKE MODEL

To reflect the dynamic characteristics of the brake, a brake dynamic model was established, which includes three stages below: disengagement, sliding, and engagement [19], [25].

$$
T_B = \begin{cases} 0, & disengagement \\ \left[\mu_{sl} + (\mu_{st} - \mu_{sl}) e^{\left(\frac{|\dot{\theta}_c| G_B}{\mu_{st} - \mu_{sl}} \right)} \right] r_B P_B A_B N_B \, \text{sgn} \left(\dot{\theta}_c \right), \\ \qquad \dot{\theta}_c \neq 0, \ sliding \\ \left[-\mu_{st} r_B P_B A_B N_B \quad \mu_{st} r_B P_B A_B N_B \right], \\ \qquad \dot{\theta}_c = 0, \ engagement \end{cases}
$$

(9)

where μ_{sl} and μ_{st} are the sliding friction coefficient and static friction coefficient of the friction plates, respectively. T_B and $\dot{\theta}_c$ are the brake torque and carrier speed, respectively. G_B, r_B, A_B and N_B are the friction gradient, effective friction radius, equivalent friction area and friction surface number, respectively. In addition, P_B is the brake oil pressure from an experimental test (shown in Fig. 9).

E. VEHICLE LONGITUDINAL DYNAMIC MODEL

The vehicle longitudinal dynamic equations are as follows [25]:

$$m\dot{V}_x = F_x - F_d - mgf \cos \beta - mg \sin \beta \quad (10)$$

$$F_d = 0.5 C_d \rho A V_x^2 sgn(V_x) \quad (11)$$

where m, V_x, F_x, F_d, g, f, β, C_d, ρ and A are vehicle mass, vehicle longitudinal speed, tire driving force, air resistance, gravitational acceleration, tire rolling resistance coefficient, road slope, air resistance coefficient, air density and vehicle frontal area.

F. POWERTRAIN MODEL VALIDATION

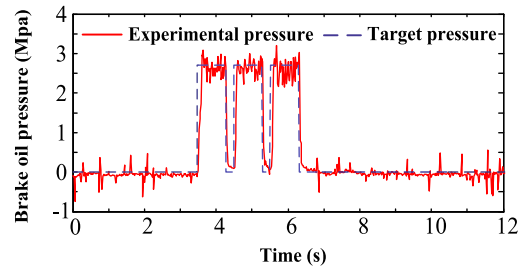Considering the spring–damping characteristics of the TDS and TI that is equivalent elastic shaft of the tire and half

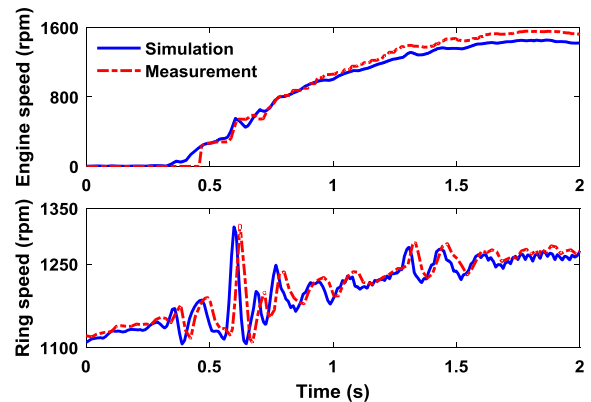**FIGURE 9.** Brake oil pressure from an experimental test.

FIGURE 10. Plant model validation.

shaft, the powertrain plant model is completed based on the above models. In order to analyze the effectiveness of the powertrain plant model, these results from simulations and experiments were compared with the same MT control strategy and parameters, as shown in Fig. 10. In the test, the vehicle accelerated to 50 km/h from standstill state, and the MT process from EV mode to ECVT mode occurred at about 32 km/h. The input variables of the plant model are the parameters from the actual acquisition, including battery state-of-charge (SOC), required torque and speed at the ring gear, engine torque, target torque and speed of the engine, engine demand angular acceleration, actual ignition speed of the engine, etc. The comparison shows that simulation results of engine speed and ring speed were in agreement with experimental results, which can verify the effectiveness of the powertrain plant model.

Most of the parameters and coefficients in the model were provided by a manufacturer, and some main parameters' values are listed in Table 1.

III. MT PROCESS AND PROBLEM DESCRIPTION

A. MT PROCESS ANALYSIS

As shown in Fig. 11, the four stages are included in the MT process: (a) EV stage with B_1 locked, (b) EV stage with B_1 being opened, (c) motoring stage before engine ignition, and (d) ECVT stage after engine ignition. Note that detailed MT conditions can be available in [28], and the relationships between speed and torque from all these stages can be available in [24].

TABLE 1. Main parameters of the vehicle powertrain.

| Parameters	Values
Engine maximum torque (Nm/rpm)	145/3600
MG1/MG2 maximum torque (Nm)	96/246
Transmission ratio of front row i_1	-3.179
Transmission ratio of rear row i_2	2.342
Final drive ratio i_0	4.044
Carrier inertia (kg·m^2)	0.0039
Ring inertia (kg·m^2)	0.0017
Inertia of MG1 and S_1 (kg·m^2)	0.041
Inertia of MG2 and S_2 (kg·m^2)	0.0723
Engine inertia (kg·m^2)	0.18
Equivalent TDS torsional stiffness (Nm·rad^{-1})	618
Equivalent TDS torsional damping (Nm·s·rad^{-1})	10
Vehicle mass (kg)	1538
Wheel radius (m)	0.31
Equivalent TI torsional stiffness (Nm·rad^{-1})	2864
Equivalent TI torsional damping (Nm·s·rad^{-1})	15
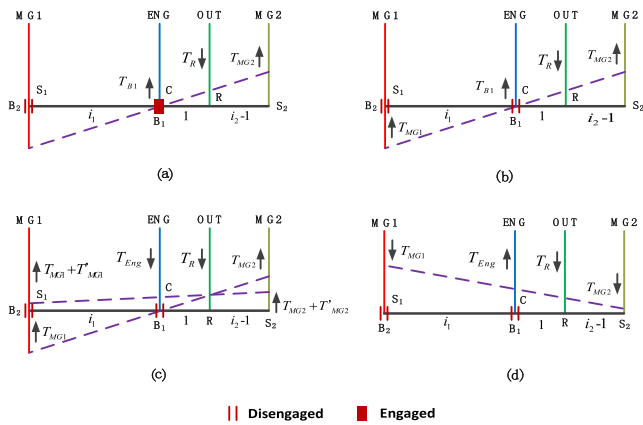
FIGURE 11. Lever diagram from EV mode to ECVT mode.

(a) In the stage 1, B_1 is locked and MG2 torque T_{MG2} will overcome the ring load torque T_R to drive the vehicle. B_1 will provide T_{B1} to balance the system. (b) In the stage 2, B_1 is quickly opened by hydraulic system. MG1 torque T_{MG1} and MG2 torque T_{MG2} will keep the engine still and drive the vehicle at the same time. (c) In the stage 3, B_1 has been fully opened, MG1 adds an torque T'_{MG1} to drag the engine to the ignition speed. MG2 adds a compensation torque T'_{MG2} to keep the vehicle running. (d) In the last stage, when the engine preset speed is reached, the engine starts ignition, and the engine torque T_{Eng} and two motors' torques will drive the vehicle together.

B. PROBLEM DESCRIPTION

The fuel economy of PS-PHEV can be effectively improved by choosing different modes. However, since a compound power-split transmission is directly connected to the engine and this transmission has no torque converter in this study, the powertrain has no passive damping as large as traditional powertrain. The ERTs in Fig. 3 and Fig. 4 will act directly on the vehicle driveline by the TDS.

As shown in Fig. 12, in the absence of DCCS, engine speed, longitudinal vibration accelerations of the seat track and
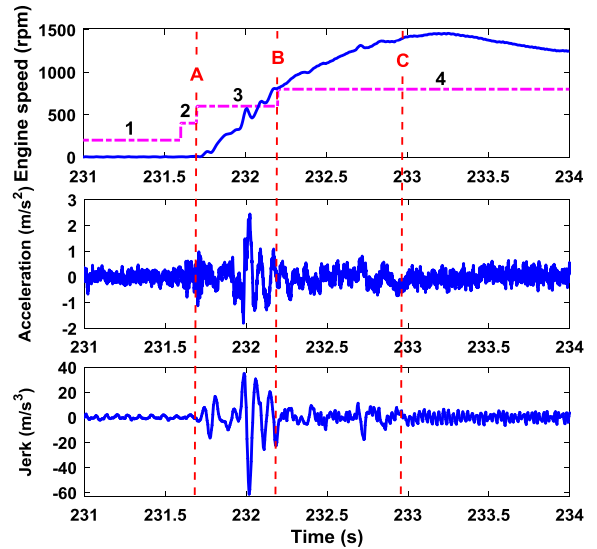

FIGURE 12. Problem description based on experimental data.

vehicle jerk during MT process from EV mode to ECVT mode at a speed of about 30km/h were gathered by using a Geely Emgrand experimentation PS-PHEV. We can see that jerks and vibrations are noticeable during motoring stage from line A to line B (engine ignition) and engine initial combustion process from line B to line C. The longitudinal vibration accelerations of the seat track was even over 2 m/s^2 and vehicle jerk was even over 60 m/s^3 during stage 3. Moreover, the obvious low-frequency fluctuations of the engine speed were generated during this process. In addition, the large shocks not only worsen the ride comfort but also affect the safety of vehicles, especially when a car is in crowded traffic.

Therefore, it is quite necessary to carry out a DCCS during the MT, especially motoring stage before ignition and engine initial combustion process after ignition, to reduce the vehicle shock and improve the driving comfort.

IV. DESIGN OF DYNAMIC COORDINATED CONTROL STRATEGY

A. SCHEMATIC DIAGRAM OF THE DCCS

In order to reduce the jerks and vibrations during the MT, a DCCS is developed, which includes "a real-time discrete motor TCRL and an ADFC with optimized DSTE." As seen in Fig. 13, three parts are mainly included in this DCCS: power source torque distribution, real-time discrete motor TCRL, and ADFC control.

Power source torque distribution mainly includes torque distributions of MG1, MG2, and the engine. MG1 torque and MG2 torque are achieved from the kinematic and dynamic equations of the vehicle powertrain obtained by the lever diagrams constructed at each stage, as shown in Fig. 11. The engine torque is obtained in accordance to the energy management control strategy [28].

The formulas describing the motor TCRL can be derived from the jerk expressions obtained by the kinematic and
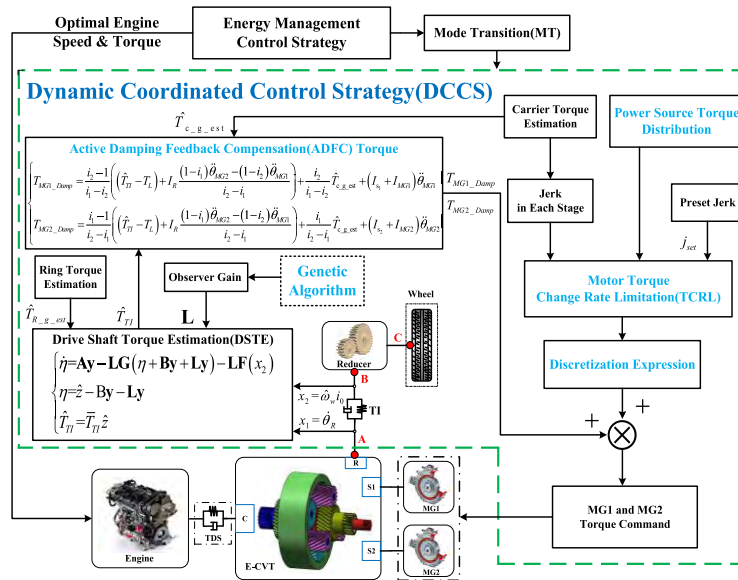
FIGURE 13. Schematic diagram of the DCCS.

dynamic equations in each stage at a preset maximum jerk. Subsequently, the limited torque change rate is discretized in time to allow its implementation in the controller. The algorithm can generally reduce the torque fluctuation transferred to the output ring (as shown at point A in Fig. 13) ,which is mainly caused by the ERT.

ADFC control includes the optimized DSTE and the ADFC torques considering MI and SPU. In order to obtain the optimal gain coefficient of DSTE to improve the robustness of the observer, error properties of active damping observer are analyzed and the DSTE gain is obtained by genetic algorithm under the constraint of linear matrix inequalities (LMIs) restriction. The ADFC control can be applied to all working stages and possess good real-time and robustness during the MT. Moreover, it can reduce the torque fluctuation transferred to the wheels (as seen at point C in Fig. 13), which is caused by MI and SPU.

The proposed DCCS above will be described in detail below.

B. POWER SOURCE TORQUE DISTRIBUTION

Torque distribution expressions of MG1 and MG2 can be derived from the kinematic and dynamic relationships of the powertrain obtained by the lever diagrams constructed at each stage, as depicted in Fig. 11.

1) EV STAGE WITH BRAKE 1 LOCKED
The torques of MG1 and MG2 can be formulated as follows:

$$
\begin{cases}
T_{MG1} = 0 \\
T_{MG2} = -T_{WH\_Lim}/(i_0 i_2) + (I_{MG2} + I_{S2}) i_0 i_2 \ddot{\theta}_{WH} \\
\qquad\quad + (i_1/i_2)(I_{MG1} + I_{S1}) i_0 i_1 \ddot{\theta}_{WH} \\
T_{B1} = -T_{WH\_Lim(i_2-1)/(i_0 i_2)}
\end{cases}
\tag{12}
$$

where T_{WH_Lim} is the demanded torque at the wheels, T_{B1} is the balance torque provided by B_1, i_1 and i_2 are the front speed ratio and rear speed ratio, i_0 is final drive ratio, I_{MG1} and I_{MG2} are the MG1 inertia and MG2 inertia, and $\ddot{\theta}_{WH}$ is the wheel angular acceleration.

2) EV STAGE WITH BRAKE 1 BEING OPENED
The torques of MG1 and MG2 are as follows:

$$
\begin{cases}
T_{MG1} = \dfrac{(i_2 - 1)\left(T_{WH\_Lim}/i_0\right) + i_2 T_{B1}}{i_1 - i_2} \\
\qquad\quad + \left(I_{s_1} + I_{MG1}\right) i_0 i_1 \ddot{\theta}_{WH} \\
T_{MG2} = \dfrac{(i_1 - 1)\left(T_{WH\_Lim}/i_0\right) + i_1 T_{B1}}{i_2 - i_1} \\
\qquad\quad + \left(I_{s_2} + I_{MG2}\right) i_0 i_1 \ddot{\theta}_{WH}
\end{cases}
\tag{13}
$$

3) MOTORING STAGE AND ECVT STAGE
Because brake 1 is fully opened at the motoring stage 3 before ignition and at the ECVT stage 4 after ignition, the dynamic equations of these two stages are the same. These two stages are described together (14), as shown at the top of the next page, where T_{Eng_des} is the engine demanded torque in accordance to the energy management control strategy [26], I_{Eng} is the engine inertia, and $\ddot{\theta}_{Eng\_des}$ is the demanded angular acceleration of the engine.

C. ALGORITHM OF MOTOR TORQUE CHANGE RATE LIMITATION

Considering the stiffness–damping characteristic of the drive shaft, the dynamic equation from the ring output shaft (point A) to the wheel (point C) can be obtained by the spring–mass model depicted in Fig. 13.

$$
T_{R_g} - T_L = I_R \ddot{\theta}_R + I_L \ddot{\theta}_L
\tag{15}
$$

$$
\begin{cases}
T_{MG1} = \dfrac{(i_2 - 1)\left(T_{WH\_Lim}/i_0\right) + i_2\left(T_{Eng\_des} - \left(I_{Eng} + I_C\right)\ddot{\theta}_{Eng\_des}\right)}{i_1 - i_2} \\
\qquad\quad + \left(I_{s_1} + I_{MG1}\right)\left(i_0 i_1 \ddot{\theta}_{WH} + (1 - i_1)\ddot{\theta}_{Eng\_des}\right) \\
T_{MG2} = \dfrac{(i_1 - 1)\left(T_{WH\_Lim}/i_0\right) + i_1\left(T_{Eng\_des} - \left(I_{Eng} + I_C\right)\ddot{\theta}_{Eng\_des}\right)}{i_2 - i_1} \\
\qquad\quad + \left(I_{s_2} + I_{MG2}\right)\left(i_0 i_2 \ddot{\theta}_{WH} + (1 - i_2)\ddot{\theta}_{Eng\_des}\right)
\end{cases}
\tag{14}
$$

where T_{R_g} is the torque at the ring gear, I_L is the equivalent inertia of TI shaft between points A and B in Fig. 13, and $\ddot{\theta}_L$ is the angular acceleration at the point B.

The formula of T_L is

$$
T_L = T_f / i_0
\tag{16}
$$

where T_f is the load torque at the wheels.

The formula used to estimate $\ddot{\theta}_R$ is as follows:

$$
\ddot{\theta}_R = \frac{(1 - i_1)\ddot{\theta}_{MG2} - (1 - i_2)\ddot{\theta}_{MG1}}{i_2 - i_1}
\tag{17}
$$

where $\ddot{\theta}_{MG1}$ and $\ddot{\theta}_{MG2}$ are the angular accelerations of MG1 and MG2, respectively.

Because the jerk, which is the second derivative of vehicle speed, can objectively and quantitatively reflect the driving comfort, it is often used as a quantitative indicator of driving comfort [29]. The expression for jerk j is as follows:

$$
j = \dddot{V}_x = \theta_L R_t / i_0
\tag{18}
$$

where θ_L is the derivative of $\ddot{\theta}_L$, and R_t is the wheel radius.

1) MOTOR TCRL
a: EV STAGE WITH BRAKE 1 LOCKED
According to (15) and Fig. 11(a), the kinetic equation of this stage can be derived with $T_{MG1} = 0$ as follows:

$$
\begin{aligned}
T_{MG2} i_2 - T_f / i_0 &= \ddot{\theta}_R \left[\left(I_{MG1} + I_{S1}\right) i_1^2 + \left(I_{MG2} + I_{S2}\right) i_2^2 + I_R\right] \\
&\quad + \ddot{\theta}_L \left(2 I_{tire} + m R_t^2\right) / i_0^2
\end{aligned}
\tag{19}
$$

where I_{tire} is the tire inertia.

Substituting the derivative of (19) into (18), the jerk of this stage can be deduced as follows:

$$
\begin{aligned}
j = \Big(i_2 \dot{T}_{MG2} - \big(&\left(I_{MG1} + I_{S1}\right) i_1^2 + \left(I_{MG2} + I_{S2}\right) i_2^2 \\
&+ I_R\big) \ddot{\theta}_R - \dot{T}_f / i_0 \Big) / I_j
\end{aligned}
\tag{20}
$$

where $\dot{T}_{MG2}$ is the torque change rate of MG2, $\ddot{\theta}_R$ is the derivative of $\ddot{\theta}_R$, $\dot{T}_f$ is the change rate of T_f, and

$$
I_j = \left(2 I_{tire} + m R_t^2\right) / (i_0 R_t)
$$

Correspondingly, $\dot{T}_f$ is defined as

$$
\dot{T}_f = \rho A C_d R_t V_x
\tag{21}
$$

In accordance to (20), the formula of $\dot{T}_{MG2}$ is

$$
\begin{aligned}
\dot{T}_{MG2} = (j_{sat} I_j + (&(I_{MG1} + I_{S1}) i_1^2 + (I_{MG2} + I_{S2}) i_2^2 \\
&+ I_R) \dddot{\theta}_R - \dot{T}_f / i_0) / i_2
\end{aligned}
\tag{22}
$$

where j_{set} is the preset jerk.

b: EV STAGE WITH BRAKE 1 BEING OPENED
According to (15) and Fig. 11(b), the kinetic equation of this stage can be derived as follows:

$$
\begin{aligned}
T_{MG1}\dot{i}_1 + T_{MG2}\dot{i}_2 &- T_f / i_0 \\
= \ddot{\theta}_R &\left[(I_{MG1} + I_{S1}) i_1^2 + (I_{MG2} + I_{S2}) i_2^2 + I_R\right] \\
&+ \ddot{\theta}_L \left(2 I_{tire} + m R_t^2\right) / i_0^2
\end{aligned}
\tag{23}
$$

Substituting the derivative of (23) into (18), the jerk of this stage can be deduced as follows:

$$
\begin{aligned}
j = (\dot{T}_{MG1} i_1 + \dot{T}_{MG2} i_2 - \dot{T}_f / i_0 - \dddot{\theta}_R ((I_{MG1} + I_{S1}) i_1^2 \\
+ (I_{MG2} + I_{S2}) i_2^2 + I_R)) / I_j
\end{aligned}
\tag{24}
$$

where $\dot{T}_{MG1}$ is the torque change rate of MG1.

In accordance to (24), the formulas of $\dot{T}_{MG2}$ and $\dot{T}_{MG1}$ under the preset jerk are as follows:

$$
\begin{aligned}
\dot{T}_{MG2} = (-\dot{T}_{MG1} i_1 + ((I_{MG1} + I_{S1}) i_1^2 + (I_{MG2} + I_{S2}) i_2^2 \\
+ I_R) \dddot{\theta}_R + \dot{T}_f / i_0 + j_{set} I_j) / i_2
\end{aligned}
\tag{25}
$$

$$
\begin{aligned}
\dot{T}_{MG1} = (-\dot{T}_{M\sigma 2} i_2 + ((I_{MG1} + I_{S1}) i_1^2 + (I_{MG2} + I_{S2}) i_2^2 \\
+ I_R) \dddot{\theta}_R + \dot{T}_f / i_0 + j_{set} I_j) / i_1
\end{aligned}
\tag{26}
$$

c: MOTORING STAGE AND ECVT STAGE
According to Fig. 11(c), Fig. 11(d), and (15), the kinetic equation of the two stages can be expressed as

$$
\begin{aligned}
\ddot{\theta}_L (2 I_{tire} &+ m R_t^2) / i_0^2 \\
&= T_{MG1} + T_{MG2} + T_{c\_axle} - \left(I_{s_1} + I_{MG1}\right)\ddot{\theta}_{MG1} \\
&\quad - (I_{s_2} + I_{MG2})\ddot{\theta}_{MG2} - I_c \ddot{\theta}_{c\_axle} - I_R \ddot{\theta}_R - T_f / i_0
\end{aligned}
\tag{27}
$$

where T_{c_axle} is the carrier torque and $\ddot{\theta}_{c\_axle}$ is the angular acceleration at the carrier axle.

The value of T_{c_axle} can be estimated from the motor torque feedback values and dynamic relationships of the planetary gears. The formula of the estimated carrier torque $\hat{T}_{c\_g\_est}$ is

$$
\begin{aligned}
\hat{T}_{c\_g\_est} = (i_1 - 1) T_{MG1} &+ (i_2 - 1) T_{MG2} \\
- (i_1 - 1)(I_{s_1} + I_{MG1})\ddot{\theta}_{MG1} &- (i_2 - 1)(I_{s_2} + I_{MG2})\ddot{\theta}_{MG2}
\end{aligned}
\tag{28}
$$

Correspondingly, the value of $\ddot{\theta}_{c\_xle}$ can be estimated as

$$\ddot{\theta}_{c\_axle} = \frac{i_2 \ddot{\theta}_{MG1} - i_1 \ddot{\theta}_{MG2}}{i_2 - i_1} \tag{29}$$

Substituting the derivative of (27) into (21) gives the deduction of the jerk of the two stages in accordance to

$$j = \left(\dot{T}_{MG1} + \dot{T}_{MG2} + \hat{T}_{c\_g\_est} - (I_{s_1} + I_{MG1}) \dddot{\theta}_{MG1} \right.$$
$$\left. - (I_{s_2} + I_{MG2}) \dddot{\theta}_{MG2} - I_c \dddot{\theta}_{c\_axle} - I_R \dddot{\theta}_R - \dot{T}_f/i_0 \right)/I_j \tag{30}$$

where $\dddot{\theta}_{c\_axle}$, $\dddot{\theta}_{MG1}$, and $\dddot{\theta}_{MG2}$ are the derivatives of $\ddot{\theta}_{c\_axle}$, $\ddot{\theta}_{MG1}$, and $\ddot{\theta}_{MG2}$, respectively, and $\dot{T}_{c\_axle}$ is the change rate of T_{c_axle}.

Using (30), the formulas of $\dot{T}_{MG2}$ and $\dot{T}_{MG1}$ under the preset jerk are derived in accordance to

$$\dot{T}_{MG2}$$
$$= -\dot{T}_{MG1} - \hat{T}_{c\_g\_est} + I_c \dddot{\theta}_{c\_axle} + (I_{s_1} + I_{MG1}) \dddot{\theta}_{MG1}$$
$$+ (I_{s_2} + I_{MG2}) \dddot{\theta}_{MG2} + I_R \dddot{\theta}_R + \dot{T}_f/i_0 + I_j j_{set} \tag{31}$$

$$\dot{T}_{MG1}$$
$$= -\dot{T}_{MG2} - \hat{T}_{c\_g\_est} + I_c \dddot{\theta}_{c\_axle} + (I_{s_1} + I_{MG1}) \dddot{\theta}_{MG1}$$
$$+ (I_{s_2} + I_{MG2}) \dddot{\theta}_{MG2} + I_R \dddot{\theta}_R + \dot{T}_f/i_0 + I_j j_{set} \tag{32}$$

2) Discretization Expression of Motor TCRL
To ensure that the motor TCRL is implemented in the controller, the limited torque change rate is discretized in time.

$$\begin{cases} Y(k) = Y(k-1) + \Delta Y \\ \Delta Y = U(k) - Y(k-1), \quad if\ \Delta_{fall\_limit} < U(k) \\ \quad - Y(k-1) < \Delta_{rise\_limit} \\ \Delta Y = \Delta_{rise\_limit} = \dot{T}_{MGi\_upper} \Delta t U(k) \\ \quad - Y(k-1) \geq \Delta_{rise\_limit} \\ \Delta Y = \Delta_{fall\_limit} = \dot{T}_{MGi\_lower} \Delta t, \quad if\ U(k) - Y(k-1) \\ \quad \leq \Delta_{fall\_limit} \end{cases} \tag{33}$$

where $Y(k)$ is the current output, $Y(k-1)$ is the output at the previous step, ΔY is the change of value at time step Δt, $U(k)$ is the input before the motor TCRL, Δ_{rise_limit} and Δ_{fall_limit} are the maximum and minimum change values during time step Δt, respectively.

D. ACTIVE DAMPING FEEDBACK COMPENSATION CONTROL
Since factors such as MI, SPU, and load changes are not considered, it is difficult for the motor TCRL algorithm to completely reduce the torque fluctuations transferred to the wheels. Therefore, a real-time robust DSTE observer is developed and used for the ADFC to effectively reduce the torque fluctuations during MT process. Moreover, genetic algorithm is used to obtain the DSTE gain under the LMIs restriction to obtain the optimal gain coefficient of DSTE to improve the robustness of the observer.

1) DESIGNED DSTE
According to the spring–mass model from the ring shaft (point A in Fig. 13) to the wheel (point C in Fig. 13) with the lumped-parameter method, we design a real-time robust DSTE observer for all working stages. This observer can estimate the drive shaft torque using the correction of angular acceleration errors based on the input-to-state stability (ISS) architecture [25], [30].

a: PROBLEM DESCRIPTION OF DSTE
As shown spring–mass model in Fig. 13, the dynamic equations are obtained:

$$T_{R\_g} - T_{TI} = I_R \ddot{\theta}_R \tag{34}$$
$$T_{TI} - T_L = I_L \ddot{\theta}_L \tag{35}$$
$$\dot{T}_{TI} = k_{TI} (\dot{\theta}_R - \dot{\theta}_L) + C_{TI} (\ddot{\theta}_R - \ddot{\theta}_L) \tag{36}$$

where T_{TI} is the actual torque of the TI shaft, k_{TI} and C_{TI} are the equivalent stiffness and damping of the tire and half shaft at the TI shaft, respectively, $\dot{\theta}_R$ is the ring speed. In addition, $\dot{\theta}_L$ is the speed of point B in Fig. 13, which can be estimated by the wheel speed estimation model.

The value of $\dot{\theta}_R$ will be obtained from planetary kinematics equation,

$$\dot{\theta}_R = \frac{(1 - i_1) \dot{\theta}_{MG2} - (1 - i_2) \dot{\theta}_{MG1}}{i_2 - i_1} \tag{37}$$

where $\dot{\theta}_{MG1}$ and $\dot{\theta}_{MG2}$ are the MG1 speed and MG2 speed, respectively.

We select $x_1 = \dot{\theta}_R$, $x_2 = \dot{\theta}_L$, and $x_3 = T_{TI}/\bar{T}_{TI}$ as state variables:

$$\dot{x}_1 = -\frac{\bar{T}_{TI}}{I_R} x_3 + f_1 \tag{38}$$

$$\dot{x}_2 = \frac{\bar{T}_{TI}}{I_L} x_3 + f_2(x_2) \tag{39}$$

$$\dot{x}_3 = \frac{k_{TI}}{\bar{T}_{TI}} (x_1 - x_2) + \frac{C_{TI}}{\bar{T}_{TI}} (\dot{x}_1 - \dot{x}_2) \tag{40}$$

where $f_1 = \frac{1}{I_R} \hat{T}_{R\_g\_est} (T_{MG1}, T_{MG2}, \ddot{\theta}_{MG1}, \ddot{\theta}_{MG2})$, $f_2(x_2) = -\frac{1}{I_L} T_L(x_2)$, and $\bar{T}_{TI}$ is the nominal setting torque of the TI axis.

The formula of the estimated ring torque $\hat{T}_{R\_g\_est}$ can be obtained:

$$\hat{T}_{R\_g\_est} = -i_1 T_{MG1} - i_2 T_{MG2} + i_1 (I_{s_1} + I_{MG1}) \ddot{\theta}_{MG1}$$
$$+ i_2 (I_{s_2} + I_{MG2}) \ddot{\theta}_{MG2} \tag{41}$$

The drive shaft torque $\hat{T}_S$ can be estimated:

$$\hat{T}_S = \hat{T}_{TI} i_0 \tag{42}$$

where $\hat{T}_{TI}$ is the estimated TI torque.

b: DESIGN OF REAL-TIME ROBUST OBSERVER
The estimated ring speed x_1 and speed x_2 of point B in Fig. 13 are combined as follows [25]:

$$\mathbf{y} = \begin{bmatrix} x_1 & x_2 \end{bmatrix}^T \tag{43}$$

We define $z(z = x_3)$ as an estimated variable, whereby the formula can be expressed as:

$$\begin{cases} \dot{y} = \mathbf{F}(x_2) + \mathbf{G}z + \mathbf{H}\omega(x_2, z) \\ \dot{z} = \mathbf{A}y + \mathbf{B}\dot{y} \end{cases} \tag{44}$$

where ω represents the model inaccuracies and uncertainties that are normalized as $\|\omega\|_\infty \approx 1$, $\mathbf{H}$ is the constant matrix obtained using ω, and

$$\mathbf{F}(x_2) = \begin{pmatrix} f_1 \\ f_2(x_2) \end{pmatrix},$$

$$\mathbf{G} = \begin{bmatrix} -\dfrac{\overline{T}_{TI}}{I_R} \\ \dfrac{\overline{T}_{TI}}{I_L} \end{bmatrix},$$

$$\mathbf{A} = \left(\dfrac{k_{TI}}{\overline{T}_{TI}}, -\dfrac{k_{TI}}{\overline{T}_{TI}} \right)$$

and

$$\mathbf{B} = \left(\dfrac{C_{TI}}{\overline{T}_{TI}}, -\dfrac{C_{TI}}{\overline{T}_{TI}} \right)$$

A real-time robust observer can be developed:

$$\dot{\hat{z}} = \mathbf{A}y + \mathbf{B}\dot{y} + \mathbf{L}\left(\dot{y} - \mathbf{F}(x_2) - \mathbf{G}\hat{z}\right) \tag{45}$$

where $\mathbf{L} \in \mathbf{R}^{1 \times 2}$ is a DSTE gain, whose physical meaning is expressed as active damping at TI axis in the controller.

We define $\eta = \hat{z} - \mathbf{B}y - \mathbf{L}y$ as an intermediate variable to reduce computational and measurement noise,

$$\dot{\eta} = \mathbf{A}y - \mathbf{L}\mathbf{G}(\eta + \mathbf{B}y + \mathbf{L}y) - \mathbf{L}\mathbf{F}(x_2) \tag{46}$$

Therefore, (46) is a real-time robust observer used to estimate drive shaft torque.

c: PROPERTIES OF DSTE OBSERVER
The errors' dynamics of this real-time robust DSTE observer are explained by using the ISS structure [30]. The observer model error is defined as

$$e = z - \hat{z} \tag{47}$$

Then, according to (14), (15) and (17), the dynamics of system errors will be expressed by

$$\begin{aligned} \dot{e} &= \mathbf{A}y + \mathbf{B}\dot{y} - \left(\mathbf{A}y + \mathbf{B}y + \mathbf{L}\left(\dot{y} - \mathbf{F}(x_2) - \mathbf{G}\hat{z}\right)\right) \\ &= -\mathbf{L}\mathbf{G}e - \mathbf{L}\mathbf{H}\omega \end{aligned} \tag{48}$$

We define $V(e) = \frac{1}{2}e^T e$ and plug (48) into its derivative to get

$$\dot{V} = -e^T \mathbf{L}\mathbf{G}e - e^T \mathbf{L}\mathbf{H}\omega \tag{49}$$

Using Young's inequalities [31], we can get

$$\dot{V} \le e^T\left(-\mathbf{L}\mathbf{G} + \kappa_1\right)e + \frac{1}{4\kappa_1}\omega^T \mathbf{H}^T \mathbf{L}^T \mathbf{L}\mathbf{H}\omega \tag{50}$$

where $\kappa_1 (\kappa_1 > 0)$ is a given static coefficient.

We will use L to satisfy the inequality as follow:

$$-\mathbf{L}\mathbf{G} + \kappa_1 \le -\kappa_2 \tag{51}$$

where $\kappa_2 (\kappa_2 > 0)$ is an error attenuation coefficient that should satisfy the required errors' decay rate [33], then we can get

$$\dot{V} \le -\kappa_2 e^T e + \frac{1}{4\kappa_1}\omega^T \mathbf{H}^T \mathbf{L}^T \mathbf{L}\mathbf{H}\omega \tag{52}$$

Moreover,

$$\dot{V} \le -\kappa_2\|e\|^2 + \frac{1}{4\kappa_1}\lambda_{\max}\left(\mathbf{H}^T \mathbf{L}^T \mathbf{L}\mathbf{H}\right)\|\omega\|_\infty^2 \tag{53}$$

Following Lemma 1 in the Appendix A, if ω is bounded, the errors' properties of the DSTE observer (45) satisfy ISS, where κ_∞ are $\rho_1(x) = \kappa_2 x^2$ and,

$$\rho_2(x) = \frac{1}{4\kappa_1}\lambda_{\max}\left(\mathbf{H}^T \mathbf{L}^T \mathbf{L}\mathbf{H}\right)x^2$$

What's more, according to (52) we can get

$$\dot{V} \le -2\kappa_2 V + \frac{1}{4\kappa_1}\omega^T \mathbf{H}^T \mathbf{L}^T \mathbf{L}\mathbf{H}\omega \tag{54}$$

We will obtain the equation after (54) is integrated,

$$\begin{aligned} V(t) \le{}& V(0)e^{-2\,x_2 t} \\ &+ \frac{1}{4\kappa_1}\int_0^t e^{-2\kappa_2(t-\tau)}\omega(\tau)^T \mathbf{H}^T \mathbf{L}\mathbf{L}\mathbf{H}\omega(\tau)d\tau \end{aligned} \tag{55}$$

Moreover,

$$\begin{aligned} \|e(t)\|^2 \le{}& \|e(0)\|^2 e^{-2\,x_2 t} + \frac{\|\omega\|_\infty^2 \lambda_{\max}\left(\mathbf{H}^T \mathbf{L}^T \mathbf{L}\mathbf{H}\right)}{2\kappa_1} \\ &\times \int_0^t e^{-2x_2(t-\tau)}d\tau \end{aligned} \tag{56}$$

Therefore, the ISS properties of the DSTE observer can be explained:
- the estimated errors' decay and stabilize exponentially with κ_2;
- as long as the maximum bound of the model error is known, the maximum bound of the estimated error can be obtained,

$$\|e(\infty)\|^2 \le \frac{\|\omega\|_\infty^2 \lambda_{\max}\left(\mathbf{H}^T \mathbf{L}^T \mathbf{L}\mathbf{H}\right)}{4\kappa_1\kappa_2} \tag{57}$$

d: DSTE GAIN FROM GENETIC ALGORITHMS
In order to obtain the optimal gain coefficient of DSTE to improve the robustness of the observer, the DSTE gain L is obtained by genetic algorithm under the LMIs restriction (58).

$$\begin{cases} \mathbf{L}\mathbf{G} - \kappa_1 - K_2 \ge 0 \\ \begin{pmatrix} \mathbf{L}\mathbf{G} - \kappa_1 - K_2 & \mathbf{L}\mathbf{H} \\ \mathbf{H}^T\mathbf{L}^T & \mathbf{I} \end{pmatrix} \ge 0 \\ K_1 > 0, K_2 > 0 \end{cases} \tag{58}$$

When ω_1 and ω_2 are step signals, the maximum bound $e_{\lim}(\infty)$ of the static errors can be obtained,

$$e_{\lim}(\infty) = \left| \frac{-a_1}{\mathbf{LG}} + \frac{-a_2}{\mathbf{LG}} \right| \qquad (59)$$

where a_j represents the jth value of LH_i.

To make the maximum bound of the estimated error close to the maximum bound of the static errors as far as possible, the fitness function F_{GA} of genetic algorithm is expressed as:

$$
\begin{aligned}
F_{GA} &= \left| \|e(\infty)\|^2 - e_{\lim}(\infty) \right| \\
&= \left| \frac{\|\omega\|_\infty^2 \lambda_{\max}\left(\mathbf{H}^T \mathbf{L}^T \mathbf{LH}\right)}{4\kappa_1\kappa_2} - \left| \frac{-a_1}{\mathbf{LG}} + \frac{-a_2}{\mathbf{LG}} \right| \right|
\end{aligned} \qquad (60)
$$

As shown in Fig. 14, the detailed steps are listed using genetic algorithm to solve the optimal gain L as follows:

Step1: load initialization conditions (**G**, **H**, **I**). **H** is determined by the errors caused by the actual possible parameters. **I** is a unit matrix.

Step2: determine an error attenuation coefficient κ_2 based on expected convergence time to satisfy the required errors' decay rate.

Step3: set up a LMIs structure based on (29) to obtain appropriate constraint conditions.

Step4: build the fitness function and set parameters of genetic algorithm such as PopulationSize, PopInitRange, CrossoverFraction and MigrationFraction. Moreover, set termination conditions such as Generations, StallGenLimit and TolFun.

By running the above steps, we can get optimal κ_1 and optimized DSTE gain L to improve the robustness of the observer.

2) ESTIMATED WHEEL SPEED

As indicated from (46), the accuracies and latencies of the estimated drive shaft torque are directly related to the wheels' speed. For the PS-PHEV studied in this paper, because of the low precision of the speed signal from the wheel speed sensor and the existence of some delay, the wheel speed signal can not satisfy the accuracy and real-time requirement of the DSTE observer [9], [10]. Therefore, it is necessary to design a wheel speed observer to estimate the wheel speed in real time. The state equation that describes the connection of the output shaft of the ring gear to the wheels is established and the discretization equations [25] are expressed as follows.

$$
\begin{cases}
\hat{\mathbf{X}}(k+1) = \begin{bmatrix} \mathbf{M} & \mathbf{0} \\ \mathbf{0} & \mathbf{I} \end{bmatrix}^{-1} \begin{bmatrix} \mathbf{C} & \mathbf{K} \\ \mathbf{I} & \mathbf{0} \end{bmatrix} \hat{\mathbf{x}}(k) \\
\qquad + \begin{bmatrix} \mathbf{M} & \mathbf{0} \\ \mathbf{0} & \mathbf{I} \end{bmatrix}^{-1} \begin{bmatrix} \mathbf{N} \\ \mathbf{0} \end{bmatrix} \mathbf{U}(k) \\
\hat{W}_{ob}(k) = \mathbf{I}_{4\times 4}(1,1)\hat{\mathbf{X}}(k)/i_0
\end{cases} \qquad (61)
$$

with

$$
\mathbf{M} = \begin{bmatrix} I_L & 0 \\ 0 & I_R \end{bmatrix}, \quad \mathbf{N} = \begin{bmatrix} -1 & 0 \\ 0 & 1 \end{bmatrix},
$$
$$
\mathbf{C} = \begin{bmatrix} -C_{TI} & C_{TI} \\ C_{TI} & -C_{TI} \end{bmatrix}
$$

and

$$
\mathbf{K} = \begin{bmatrix} -k_{TI} & k_{TI} \\ k_{TI} & -k_{TI} \end{bmatrix}
$$

where $\hat{X}$ is the estimated state variable, U is the control variable, I is the unit matrix, $\hat{W}_{ob}$ is the estimated wheel speed, and k is the sample number.

3) ADFC TORQUES

The ADFC torques ($T_{MG1_{Damp}}$ and $T_{MG2_{Damp}}$) of MG1 and MG2 can be deduced by the lever diagram in Fig. 11.

$$
\begin{aligned}
T_{MG1\_Damp} &= \frac{i_2 - 1}{i_1 - i_2}\left(\left(\hat{T}_{TI} - T_L \right) \right. \\
&\quad \left. + I_R \frac{(1-i_1)\ddot{\theta}_{MG2} - (1-i_2)\ddot{\theta}_{MG1}}{i_2 - i_1} \right) \\
&\quad + \frac{i_2}{i_1 - i_2}\hat{T}_{c\_g\_est} + \left(I_{s_1} + I_{MG1} \right)\ddot{\theta}_{MG1} \quad (62) \\
T_{MG2\_Damp} &= \frac{i_1 - 1}{i_2 - i_1}\left(\left(\hat{T}_{TI} - T_L \right) \right. \\
&\quad \left. + I_R \frac{(1-i_1)\ddot{\theta}_{MG2} - (1-i_2)\ddot{\theta}_{MG1}}{i_2 - i_1} \right) \\
&\quad + \frac{i_1}{i_2 - i_1}\hat{T}_{c\_g\_est} + \left(I_{s_2} + I_{MG2} \right)\ddot{\theta}_{MG2} \quad (63)
\end{aligned}
$$

In equations (35) and (36), the ADFC torques can be obtained by plugging the estimated torque $\hat{T}_{TI}$ at TI axis from DSTE and estimated carrier torque $\hat{T}_{c\_g\_est}$ into equations (35) and (36). The ADFC torques can reduce the fluctuating torques transferred to the wheels to further reduce the shock and vibration of the vehicle transmission system.

V. SIMULATIONS AND DISCUSSION

A. SIMULATION INTRODUCTION

In order to confirm whether the accuracy of DSTE observer satisfies the requirements of the proposed DCCS, the accuracy of DSTE is first verified by using the powertrain plant model during MT. To compare and analyze the control effectiveness, three control methods are introduced: 1) baseline control (BC) method without coordinated control, 2) motor TCRL only, 3) proposed motor TCRL and DSTE-based ADFC (TCRL–ADFC).

B. DSTE RESULTS

According to the assumptions in Table 2, we can get $H = \begin{pmatrix} 14.8 & 0 \\ 0 & 28.55 \end{pmatrix}$. Following the steps of genetic algorithm under the LMIs restriction in Fig. 14 and parameters of genetic algorithm in Table 2, we can see that when $\kappa_1 = 25.45$ in Fig. 15, an optimal DSTE gain $L = \begin{pmatrix} -1.4041 & 0.0227 \end{pmatrix}$

TABLE 2. Calculation conditions.

Categories	Parameters	Values
Assumption conditions	Nominal setting torque (Nm)	500
	Error attenuation coefficient	400
	Estimated ring torque error	±5%
	Estimated wheel speed error	±5%
	Vehicle mass (kg)	1530-2000
	Road slope (%)	0-9
Main parameters of genetic algorithm	PopulationSize	80
	Generations	30
	TolFun	1e-6
	CrossoverFraction	0.4
	MigrationFraction	0.1

FIGURE 15. Convergence results of genetic algorithm.

FIGURE 14. Flow diagram of genetic algorithm under LMIs restriction.
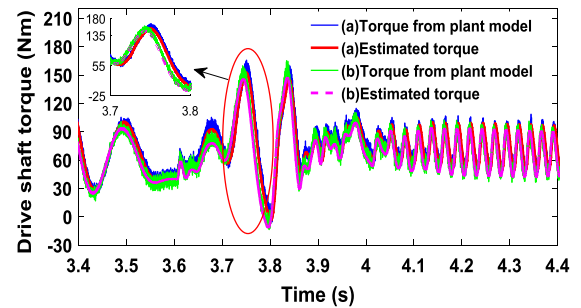
FIGURE 16. DSTE results.
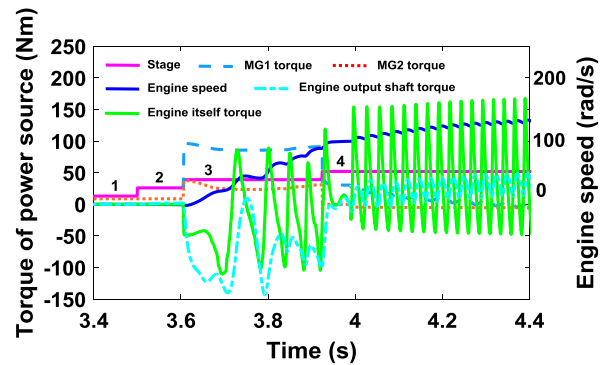
FIGURE 17. Dynamics of power source at different stages using BC.

is obtained to improve observer robustness. The maximum bound of the static errors for all working stages is $|e(\infty)| \leq e_{\lim}(\infty) = 0.017$. The maximum drive shaft torque error is $0.0166 \times \bar{T}_{TI} \times i_0 = 33.57$ Nm, which is less than 3% of the maximum drive shaft torque that meets the requirements of DCCS applications.

As shown in Fig. 16, the drive shaft torques are obtained during the MT process at 30 km/h. Under the conditions of (a) m=1530kg, $\beta = 0$; (b) m=2000kg, $\beta = 9\%$, the comparison shows that estimated results for drive shaft torques were in agreement with those from the powertrain plant model, which verifies the effectiveness of the DSTE observer. Moreover, these results show that the DSTE observer possesses good real-time and robustness during the MT, which can meet the requirements of ADFC control system.

C. RESULT ANALYSIS OF DCCS

Under the EV mode with B_1 locked, the vehicle is running at 30km/h. Assuming that SOC is less than the preset threshold at 3.5s, the vehicle begins to enter the MT process from EV mode to ECVT mode.

As shown in Fig. 17, the dynamics of power source are obtained by using BC method. Two motors start to drag the engine to reach the preset ignition speed (850rpm) when stage 3 is entered. We can see that the ERTs before engine flywheel show obvious fluctuations, which also cause significant fluctuations of engine output shaft torque. Finally, these
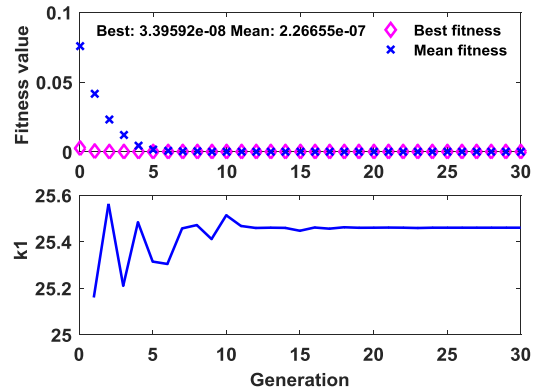
ERTs cause the significant low-frequency fluctuations of engine speed during stage 3 and engine initial ignition process in the fourth stage.

As shown in Figs. 18 and 19, the limited areas of torque change rates of the two motors between the lower and upper bounds are obtained by the motor TCRL algorithm at the preset maximum jerk $J_{a-\max} = 7m/s^3$. As illustrated in Figs. 20 and 21, MG1 torque command and MG2 torque command can be obtained by using these three DCCS mentioned above. Besides, the ADFC torques of the two motors are produced by using the TCRL-ADFC method to minimize torque fluctuations caused by MI and SPU, as shown in Fig. 22.
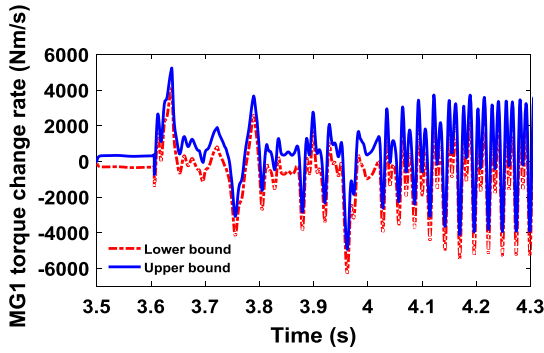
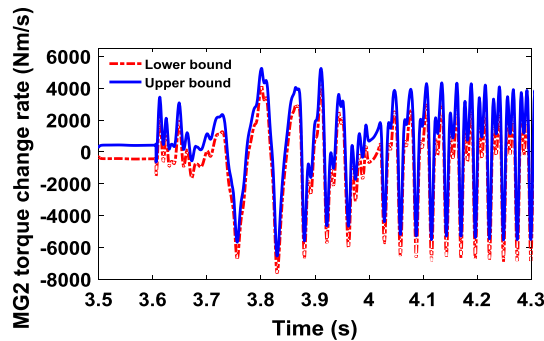FIGURE 18. MG1 torque change rate limitation.
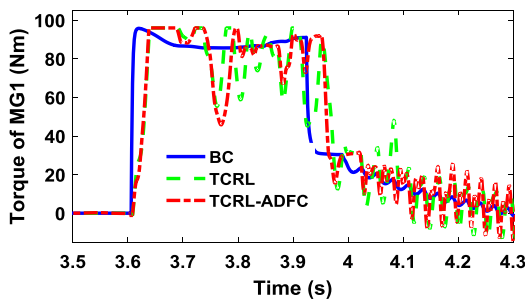

FIGURE 19. MG2 torque change rate limitation.
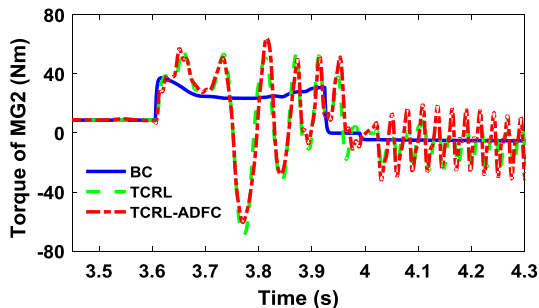

FIGURE 20. MG1 target torque commands.

FIGURE 21. MG2 target torque commands.

FIGURE 22. Active damping feedback compensation torque.
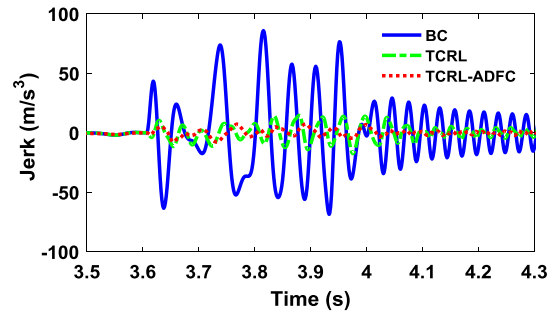
FIGURE 23. Vehicle jerk.

FIGURE 24. Vehicle ARMS.

Figs. 23 and 24 and Table 4 show the comparative analysis results among these three different dynamic control strategies. We can find that compared to the BC strategy, J_{a-max} obtained by using the real-time TCRL control method
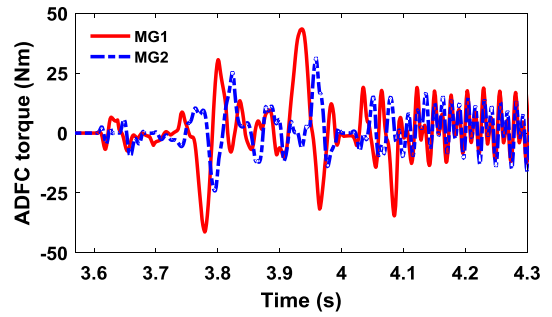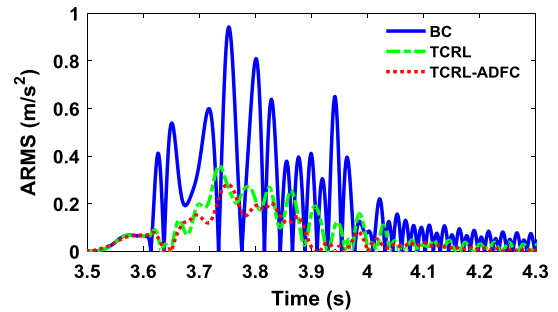
is controlled from 85.91 m/s^3 to 17.5 m/s^3, and this method yields a jerk improvement of 79.63%. Note that J_{a-max} denotes the absolute value of maximum vehicle jerk. But the jerk is not reduced to the preset value of 7 m/s^3. On the other hand, J_{a-max} from the proposed TCRL–ADFC strategy is reduced to 7.02 m/s^3, with a better jerk improvement of 91.83% compared to the BC strategy and an improvement of 59.89% compared to the TCRL method. Moreover, $A_{RMS-max}$ obtained by using the TCRL–ADFC strategy is the lowest, and the fluctuations of the maximum values for the acceleration root-mean-square (ARMS) are more stable than the other two methods. Note that $A_{RMS-max}$ is the maximum ARMS value.

Fig. 25 demonstrates the frequency spectrum of the jerk data between 4.1 s and 4.3 s in Fig. 23. We see that the fluctuation frequency of the vehicular jerk is equal to the fluctuation frequency (40 Hz) of the ERT in the same duration

TABLE 3. Cases for TCRL–ADFC robustness verification.

Categories	Parameters	Case 1	Case 2	Case 3
System parameter uncertainties (SPU)	TDS equivalent damping (Nm·s·rad^{-1})	5	10	5
	TI shaft equivalent damping (Nm·s·rad^{-1})	13.5	15	13.5
	Vehicle mass (kg)	1530	1830	2000
	Road slope (%)	0	5	9
Model inaccuracies (MI)	Carrier torque estimation error	3%	5%	5%
	B$_1$ torque error	4%	4%	4%
	Wheel speed estimation error	3%	5%	5%
	Ring torque estimation error	3%	5%	5%

TABLE 4. Results of DCCS during the MT process.

Control methods	J$_{a\text{-}max}$ (m/s^3)	Improvement of J$_{a\text{-}max}$ (%)	A$_{RMS\text{-}max}$ (m/s^2)	Improvement of A$_{RMS\text{-}max}$ (%)
BC	85.91	—	0.94	—
TCRL	17.5	79.63	0.389	58.62
TCRL–ADFC	7.02	91.83	0.28	70.21

Note that J$_{a\text{-}max}$ is the absolute value of maximum vehicle jerk, and A$_{RMS\text{-}max}$ is the maximum ARMS value.

TABLE 5. Experimental cases for TCRL–ADFC robustness verification.

Categories	Parameters	Case 1	Case 2	Case 3
System parameter uncertainties (SPU)	TI shaft equivalent damping in the algorithm (Nm·s·rad^{-1})	13.5	15	13.5
	Vehicle mass (persons)	1	3	5
	Road slope (%) (random)	0-9	0-9	0-9
Model inaccuracies (MI)	Carrier torque estimation error	3%	5%	5%
	Wheel speed estimation error	3%	5%	5%
	Ring torque estimation error	3%	5%	5%

FIGURE 25. Frequency spectrum of jerk from 4.1 s to 4.3 s.

FIGURE 26. TCRL–ADFC robustness verification.

in Fig. 17. This result also indicates that the jerk is mainly caused by the ERT. Moreover, compared to the BC and TCRL methods, the TCRL–ADFC method effectively reduces fluctuation amplitude of the jerk in Fig. 25.

For Table 3 and Table 5, the MI is expressed as the range of the error of model or model estimation, whose quantitative value is used to represent the upper limit of the maximum error. Based on these main parameters of the SPU and MI for the compound PS-PHEV, three cases are designed in Table 3 to analyze whether the proposed DCCS has better robustness against system disturbance factors using the multivariate analysis method.

Fig. 26 demonstrates the comparative simulation results of these three cases using the TCRL and TCRL–ADFC methods. It is proved that vehicle jerks are different under
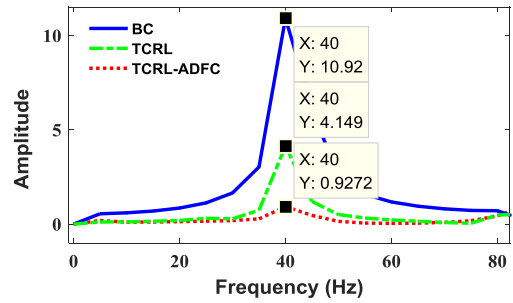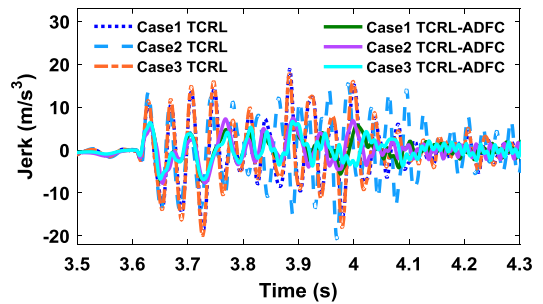
different cases. Then, it is seen that the two motor compensation torques resulting from the TCRL method cannot completely compensate the torque ripple of the system, and the jerk cannot meet the design requirement (i.e., the preset value 7 m/s^3). However, the jerk resulting from the TCRL–ADFC method is effectively suppressed to about 7 m/s^3 at each case. These results show that the proposed DCCS has strong robustness against SPU and MI and it has been proved that it can effectively reduce the shocks and vibrations of the vehicle transmission system and improve the driver comfort.

VI. EXPERIMENTAL RESULTS AND DISCUSSION

A series of experiments were carried out with a Geely Emgrand experimentation PS-PHEV. The main parameters related to the PS-PHEV are listed in Table 1. Vibration acceleration sensors were mounted on the driver's seat rail and steering wheel to collect the longitudinal accelerations of the vehicle. The host computer was connected with the controller area network (CAN) signal transfer box for debugging and loading control strategy. The signal acquisition system was used to collect data from acceleration sensors and CAN signal transfer box. In the test, the vehicle accelerated to 50 km/h from standstill state with full acceleration pedal, and when the vehicle speed reached 30 km/h, the powertrain mode was changed from EV mode to ECVT mode. The experimental environment was shown in Fig. 27.

As shown in Fig. 28, the dynamics of power source were obtained by using the proposed TCRL-ADFC method. It consists of four stages, which are the same as simulation. The proposed method was implemented only in the third stage
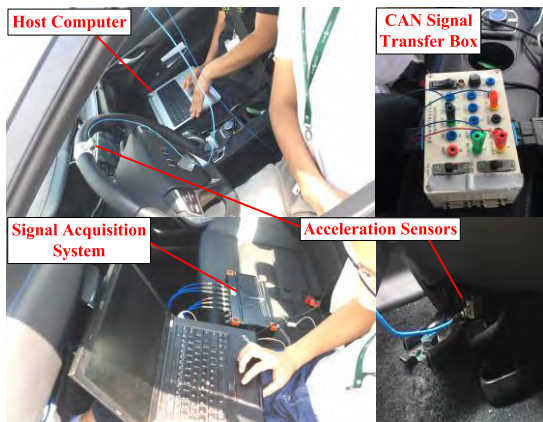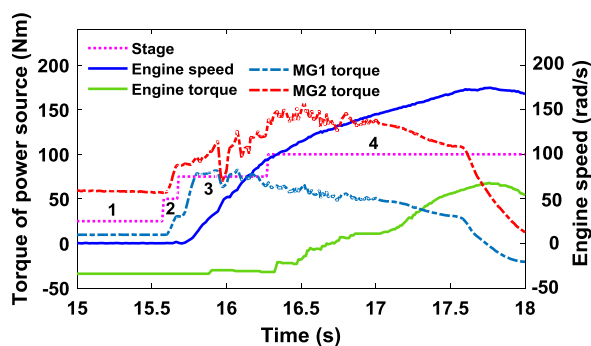
FIGURE 27. Experiment environment.

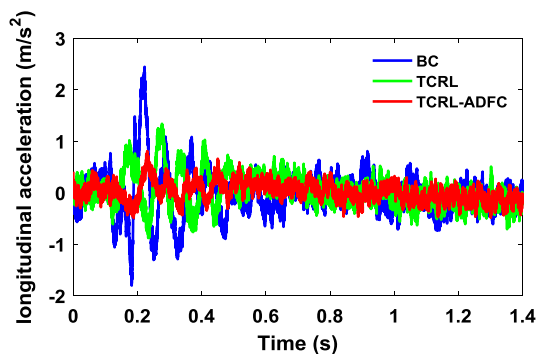FIGURE 28. Dynamics of power source using the TCRL-ADFC.

FIGURE 29. Longitudinal vibration accelerations of the seat track.

FIGURE 30. Vehicle jerk.

FIGURE 31. Longitudinal vibration accelerations of the seat track.

FIGURE 32. Vehicle jerk for cases.

and engine initial combustion process after the injection flag at 16.27s. Torques of two motors with significant changes were performed to offset the ripple torque produced by the system. And the engine speed was smooth before and after injection flag at 16.27s.

To better analyze the experimental data, the time axis of the data in stage 2, stage 3 and engine initial combustion process in stage 4 was converted to 0-1.4s, as shown in Figs. 29-32. The longitudinal vibration accelerations of the seat track were used to evaluate three methods, as shown in Fig. 29. Compared to the BC strategy, A_{cc-max} obtained
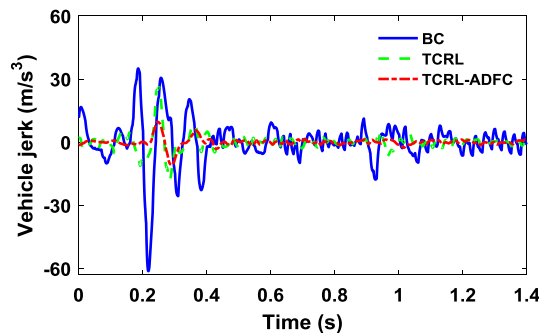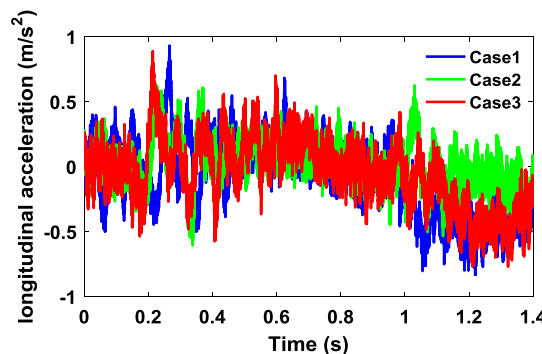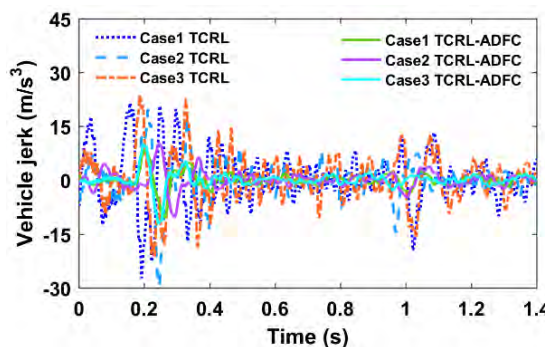
by using the TCRL control strategy was decreased from 2.447 m/s^2 to 1.32 m/s^2, giving a jerk improvement of 46.06%. Note that A_{cc-max} is the absolute value of maximum longitudinal vibration acceleration. On the other hand, A_{cc-max} from the TCRL–ADFC strategy was decreased to 0.745 m/s^2, showing a better jerk improvement of 69.55% compared to the BC strategy and an improvement of 43.56% compared to the TCRL method, as seen from Table 6. Fig. 30 and Table 6 demonstrated the comparative vehicle jerk results among the different dynamic control strategies. We could find that compared to the BC strategy, J_{a-max} from the TCRL strategy was controlled from 61.18 m/s^3 to 26.11 m/s^3, presenting a better jerk improvement of 57.32%. But the jerk was not reduced to the preset value of 10 m/s^3. On the other hand, J_{a-max} obtained using the TCRL–ADFC

TABLE 6. Experimental results of DCCS.

Control methods	$A_{cc\text{-}max}$ (m/s^2)	Improvement of $A_{cc\text{-}max}$ (%)	$J_{a\text{-}max}$ (m/s^3)	Improvement of $J_{a\text{-}max}$ (%)
BC	2.447	—	61.18	—
TCRL	1.32	46.06	26.11	57.32
TCRL–ADFC	0.745	69.55	10.85	82.27

Note that $A_{cc\text{-}max}$ is the absolute value of maximum longitudinal vibration acceleration.

strategy was further reduced to 10.85 m/s^3, with a better jerk improvement of 82.27% compared to the BC strategy and an improvement of 58.45 % compared to the TCRL method.

To analyze whether the proposed DCCS has good robustness against system disturbance factors, the three cases used for experiments had been conducted in Table 5. As seen in Fig. 31, longitudinal accelerations of the seat track of these three cases were controlled within 0.9 m/s^2 using TCRL–ADFC. Moreover, Fig. 32 demonstrated the comparative experimental results of three cases using the TCRL and TCRL–ADFC methods. The jerk resulting from the TCRL–ADFC method could be effectively suppressed to about 10 m/s^3 at each case during the MT process. These results indicated that the proposed control method had strong robustness against SPU and MI. It was proved that it could effectively reduce the shocks and vibrations of the vehicle transmission system and improve the driver comfort.

VII. CONCLUSIONS

In order to improve the ride comfort of drivers, this study proposed a dynamic coordinated control strategy that synergizes real-time discrete motor TCRL and ADFC with DSTE for a compound PS-PHEV. A detailed vehicle powertrain simulation model was established and validated. The relevant problems in the MT were analyzed by experimental data. The formulas of the power source torque distribution and real-time discrete motor TCRL were derived from the kinematic and dynamic equations of the powertrain at each stage. Considering the model inaccuracies, system parameter uncertainties, and load changes, an ADFC based on a real-time robust DSTE observer was designed. Moreover, the optimal DSTE gain was obtained by genetic algorithm under the LMIs restriction to improve the robustness of the observer. Finally, the BC, TCRL, and proposed TCRL–ADFC methods were employed for comparative analyses. The results from simulations and experiments showed that the proposed method could effectively improve the drivers' driving comfort and possessed good real-time robustness against disturbances during MT process. In addition, the proposed DCCS has good universality in theory and can also be used in other MT processes, such as two-motor torque switching, engine shutdown process.

APPENDIX A
Lemma 1: For a system

$$\dot{x} = f(x, w) \tag{64}$$

system properties present equivalent states below [30], [32]:

TABLE 7. Abbreviations listed in the text.

Abbreviations	Explanations
ADFC	Active damping feedback compensation
ARMS	Acceleration root-mean-square
BC	Baseline control
CAN	Controller area network
DCCS	Dynamic coordinated control strategy
DSTE	Drive shaft torque estimation
ECVT	Electric continuous variable transmission
ERT	Engine ripple torque
EV	Electric vehicle
ISS	Input-to-state stability
LMIs	Linear matrix inequalities
MG1	Small motor 1
MG2	Big motor 2
MI	Model inaccuracies
MT	Mode transition
PD	Proportion and differentiation
PM	Permanent magnet
PS-PHEV	Power-split plug-in hybrid electric vehicle
SOC	State of charge
SPS	Simscape power system
SPU	System parameter uncertainties
TCRL	Torque change rate limitation
TDS	Torsional damper spring
TI	Equivalent elastic shaft of the tire and half shaft

- the system obeys ISS structure;
- there is a C^1 formula V: $\mathbf{R}^n \rightarrow \mathbf{R}_+$, for all variables $x \in \mathbf{R}^n$ and $\omega \in \mathbf{R}^m$,

$$\gamma_1(|x|) \leq V(x) \leq \gamma_2(x)$$
$$|x| \geq \rho(|\omega|) \Rightarrow \frac{\partial V}{\partial x} f(x, \omega) \leq -\gamma_3(|x|)$$

where γ_1, γ_2, and ρ stand for functions of class κ_∞ and γ_3 denotes a function of class κ.
- there is a positive definite and unbounded function V and functions ρ_1 and ρ_2 of class κ_∞ so that dissipativity inequalities below are met:

$$\frac{\partial V}{\partial x} f(x, \omega) \leq -\rho_1(|x|) + \rho_2(|\omega|).$$

APPENDIX B
See Table 7.

REFERENCES

[1] G. Wu, X. Zhang, and Z. Dong, "Powertrain architectures of electrified vehicles: Review, classification and comparison," *J. Franklin Inst.*, vol. 352, no. 2, pp. 425–448, Feb. 2015.

[2] X. Zhang, S. E. Li, H. Peng, and J. Sun, "Efficient exhaustive search of power-split hybrid powertrains with multiple planetary gears and clutches," *J. Dyn. Syst. Meas. Control*, vol. 137, no. 12, Dec. 2015, Art. no. 121006.

[3] O. H. Dagci, H. Peng, and J. W. Grizzle, "Hybrid electric powertrain design methodology with planetary gear sets for performance and fuel economy," *IEEE Access*, vol. 6, pp. 9585–9602, 2018.

[4] J. Wu, J. Ruan, N. Zhang, and P. D. Walker, "An optimized real-time energy management strategy for the power-split hybrid electric vehicles," *IEEE Trans. Control Syst. Technol.*, vol. 27, no. 3, pp. 1194–1202, May 2018.

[5] M. L. Kuang, "An investigation of engine start-stop NVH in a power split powertrain hybrid electric vehicle," SAE Tech. Paper 2006-01-1500, 2006.

[6] H.-Y. Hwang, "Minimizing seat track vibration that is caused by the automatic start/stop of an engine in a power-split hybrid electric vehicle," *J. Vib. Acoust.*, vol. 135, no. 6, Dec. 2013, Art. no. 061007.

[7] J.-S. Chen and H.-Y. Hwang, "Engine automatic start–stop dynamic analysis and vibration reduction for a two-mode hybrid vehicle," *Proc. Inst. Mech. Eng. D, J. Automobile Eng.*, vol. 227, no. 9, pp. 1303–1312, Sep. 2013.

[8] D. Liu, J. Zhang, D. Zhang, G. Liu, and H. Yu, "Experimental and numerical analysis of the seat track vibrations caused by engine starts in a power-split hybrid electric vehicle," *Proc. Inst. Mech. Eng. D, J. Automobile Eng.*, vol. 231, no. 3, pp. 395–404, Feb. 2017.

[9] M. Canova, Y. Guezennec, and S. Yurkovich, "On the control of engine start/stop dynamics in a hybrid electric vehicle," *J. Dyn. syst., Meas., Control*, vol. 131, no. 6, Nov. 2009, Art. no. 061005.

[10] R. I. Davis and R. D. Lorenz, "Engine torque ripple cancellation with an integrated starter alternator in a hybrid electric vehicle: Implementation and control," *IEEE Trans. Ind. Appl.*, vol. 39, no. 6, pp. 1765–1774, Nov./Dec. 2003.

[11] S. Tomura, Y. Ito, K. Kamichi, and A. Yamanaka, "Development of vibration reduction motor control for series-parallel hybrid system," SAE Tech. Paper 2006-01-1125, 2006.

[12] C. Wang, Z. Zhao, T. Zhang, and M. Li "Mode transition coordinated control for a compound power-split hybrid car," *Mech. Syst. Signal Process.*, vol. 87, pp. 192–205, Mar. 2017.

[13] X. Zeng *et al.*, "Predictive-model-based dynamic coordination control strategy for power-split hybrid electric bus," *Mech. Syst. Signal Process.*, vols. 60–61, pp. 785–798, Aug. 2015.

[14] X. Zeng, Y. Wang, D. Song, L. Zhu, and G. Tian "Coordinated control algorithm of a dual motor for an electric variable transmission hybrid system," *IEEE Access*, vol. 6, pp. 35669–35682, 2018.

[15] W. Zhuang, D. Kum, H. Peng, L. Wang, and D. Li, "Optimal engine starts of an input-split hybrid electric vehicle," *SAE Int. J. Alternative Powertrains*, vol. 4, no. 2, pp. 343–351, Jul. 2015.

[16] Z. Zhao, L. Jiang, C. Wang, and M. Li, "Engine start-up optimal control for a compound power-split hybrid powertrain," *Mech. Syst. Signal Process.*, vol. 120, pp. 365–377, Apr. 2019.

[17] F. U. Syed, M. L. Kuang, and H. Ying, "Active damping wheel-torque control system to reduce driveline oscillations in a power-split hybrid electric vehicle," *IEEE Trans. Veh. Technol.*, vol. 58, no. 9, pp. 4769–4785, Nov. 2009.

[18] H. Kim, J. Kim, and H. Lee, "Mode transition control using disturbance compensation for a parallel hybrid electric vehicle," *Proc. Inst. Mech. Eng. D, J. Automobile Eng.*, vol. 225, no. 2, pp. 150–166, Feb. 2011.

[19] L. Wang, Y. Zhang, J. Shu, and C. Yin, "Mode transition control for series-parallel hybrid electric bus using fuzzy adaptive sliding mode approach," *Jixie Gongcheng Xuebao Chin. J. Mech. Eng.*, vol. 48, no. 14, pp. 119–127, Jul. 2012.

[20] C. Yang, L. Li, X. Jiao, Y. Zhang, Z. Chen, and J. Song, "Research on mode transition control for single-shaft parallel hybrid powertrain," *Scientia Sinica Technol.*, vol. 46, no. 1, pp. 91–100, Dec. 2016.

[21] H. Zhang, C. L. Wang, Y. Zhang, J. Y. Liang, and C. L. Yin, "Drivability improvements for a single-motor parallel hybrid electric vehicle using robust controls," *J. Zhejiang Univ.-Sci. A*, vol. 15, no. 4, pp. 291–301, Apr. 2014.

[22] H. Zhang, Y. Zhang, and C. Yin, "Hardware-in-the-loop simulation of robust mode transition control for a series–parallel hybrid electric vehicle," *IEEE Trans. Veh. Technol.*, vol. 65, no. 3, pp. 1059–1069, Mar. 2016.

[23] B. Zhou, J. Zhang, J. Gao, H. Yu, and D. Liu, "Clutch pressure estimation for a power-split hybrid transmission using nonlinear robust observer," *Mech. Syst. Signal Process.*, vol. 106, pp. 249–264, Jun. 2018.

[24] Y. Su, M. Hu, L. Su, D. Qin, T. Zhang, and C. Fu, "Dynamic coordinated control during mode transition process for a compound power-split hybrid electric vehicle," *Mech. Syst. Signal Process.*, vol. 107, pp. 221–240, Jul. 2018.

[25] Z. Zhi, X. Dai, C. Wang, T. Zhang, and X. Yuan, "Coordinated control of driving mode switching of compound power-split hybrid electric car," *Automotive Eng.*, vol. 37, no. 3, pp. 260–265, 2015.

[26] D. Yuan, Y. Xu, and X. Li, *Variable Frequency System of Permanent Magnet Synchronous Motor and Control*. Mechanical Industry Press, 2015. [Online]. Available: http://xueshu.baidu.com/usercenter/paper/show?paperid=d080fadc092be6395e3d6a50ec54a8c3&site=xueshu_se&hitarticle=1

[27] Y. Su, M. Hu, L. Su, D. Qin, and Y. Liu, "Study on dynamic characteristics of electromechanical coupling in mode switching process of multi-power transmission system considering internal and external excitation," in *Proc. JSME Int. Conf. Motion Power Transmiss.*, 2017, p. 10.

[28] H.-S. Yu, J. W. Zhang, and T. Zhang, "Control strategy design and experimental research on a four-shaft electronic continuously variable transmission hybrid electric vehicle," *Proc. Inst. Mech. Eng. D, J. Automobile Eng.*, vol. 226, no. 12, pp. 1594–1612, Dec. 2012.

[29] X. Wei, P. Pisu, G. Rizzoni, and S. Yurkovich, "Dynamic modeling of a hybrid electric drivetrain for fuel economy, performance and driveability evaluations," in *Proc. ASME Int. Mech. Eng. Congr. Expo.*, Jan. 2003, pp. 443–450.

[30] E. D. Sontag, "Input to state stability: Basic concepts and results," *Nonlinear and Optimal Control Theory*. Berlin, Germany: Springer, 2008, pp. 163–220.

[31] M. Krstic, I. Kanellakopoulos, and P. Kokotovic, *Nonlinear and Adaptive Control Design*. New York, NY, USA: Wiley, 1995.

[32] B. Gao, H. Chen, Y. Ma, and K. Sanada, "Design of nonlinear shaft torque observer for trucks with automated manual transmission," *Mechatronics*, vol. 21, no. 6, pp. 1034–1042, Sep. 2011.

[33] K. Ogata, *Modern Control Engineering*, 4th ed. Upper Saddle River, NJ, USA: Prentice-Hall, 2014.

YANZHAO SU was born in Zhengzhou, Henan, China. He received the M.S. degree in vehicle engineering from Chongqing Jiaotong University, Chongqing, China, in 2015, where he is currently pursuing the Ph.D. degree in vehicle engineering. He is also pursuing the Ph.D. degree with the University of Michigan–Dearborn, Dearborn, MI, USA.

He has published several papers on hybrid cars, and he has applied for 13 national invention patents on the configurations of hybrid electric vehicles. He participates in the National Natural Science Foundation of China and the National Key Research and Development Project. His research interests include the design, analysis, and control of power transmission systems.

MINGHUI HU was born in Xi'an, China. He received the B.S., M.S., and Ph.D. degrees in mechanical engineering from Chongqing University, in 1998, 2003, and 2007, respectively, where he has been a Professor with the School of Automotive Engineering, since 2017.

He has over seventeen years of extensive experience in the field of vehicle power transmission systems, since 2000. He has been leading or participated in over 70 research projects. He has published over ninety academic papers, which are published in prestigious journals. He is the owner of over 30 invention patents. He has received the Local Government Prize and the China South Industries Group Corporation Prize for his research achievements in the fields of vehicle powertrain systems.

LING SU was born in Chongqing, China. He received the B.S., M.S., and Ph.D. degrees in mechanical engineering from Xi'an Jiaotong University, in 1998, 2001, and 2005, respectively.

He is a Senior Engineer in new energy vehicle with Chongqing Changan Automobile Co., Ltd., and the Deputy General Manager of Changan New Energy Automobile Co., Ltd. He has over 13 years of extensive experience in the field of new energy vehicle, since 2005. He has been leading or participated in over ten research projects. He has published over ten academic papers. He is the owner of over 35 invention patents. He has received many honors, such as the China Auto Industry Science and Technology Award, the Chongqing Technology Invention Award, and the Chongqing Science and Technology Progress Award.

DATONG QIN was born in Chongqing, China, in 1956. He received the B.S., M.S., and Ph.D. degrees in mechanical engineering from Chongqing University, in 1982, 1984, and 1993, respectively, where he has been the Vice Dean (part-time) of the Graduate School, since 2009.

He was a Visiting Scholar with the Department of Precision Engineering, Tohoku University, Japan, from 1989 to 1991. He was the Deputy Director of the SKLMT, China, from 1995 to 1997, where he is also the Director, from 1997 to 2008. He was appointed by the Ministry of Education of China as the Changjiang Chair Professor, in 2005. His fields of research include powertrain systems for conventional vehicles and hybrid electric vehicles, gearing theory, and gearing transmission systems. He has published over two hundreds of academic papers, which have been published in national and international journals or presented at national and international conferences. He is the owner of over twenty invention patents. He has received two national prize from the Central Government of China and 11 prizes from the Ministry of Education or local government for his research achievements in the areas of powertrain systems of vehicles and gear transmission.

YI ZHANG received the B.S. degree in mechanical engineering from Central South University, Changsha, China, in 1982, and the M.S. and Ph.D. degrees in mechanical engineering from the University of Illinois at Chicago, Chicago, USA, in 1985 and 1989, respectively.

He is currently a Professor with the Department of Mechanical Engineering, University of Michigan–Dearborn, Dearborn, MI, USA. He has published dozens of academic papers in his research areas. He has also published a book *Automotive Power Transmission Systems* (John Wiley and Sons, 2018). His areas of interest include the design and analysis of gearing systems, theory of gearing and applications, vehicle powertrains, and the design and analysis of power transmission systems.

● ● ●